Triggering of the powerful 14 July 2013 Vulcanian explosion at Tungurahua Volcano, Ecuador

H. Elizabeth Gaunt [a,*], Alain Burgisser [b], Patricia A. Mothes [a], John Browning [c], Philip G. Meredith [d], Evelyn Criollo [e], Benjamin Bernard [a]

[a] Instituto Geofísico, Escuela Politécnica Nacional, Quito, Ecuador.
[b] Univ. Grenoble Alpes, Univ. Savoie Mont Blanc, CNRS, IRD, IFSTTAR, ISTerre, 38000 Grenoble, France
[c] Department of Mining Engineering and Department of Structural and Geotechnical Engineering Pontificia Universidad Católica de Chile, Chile
[d] Rock and Ice Physics Laboratory, Department of Earth Science, University College London, London, UK
[e] Departamento de Metalurgia Extractiva, Escuela Politécnica Nacional, Quito, Ecuador

ARTICLE INFO

ABSTRACT

The 14 July 2013 Vulcanian explosion at Tungurahua occurred after two months of quiescence and was extremely powerful, generating some of the highest infrasound energies recorded worldwide. Here we report on how a combination of geophysical data, textural measurements, and physical and mechanical tests on eruptive products allowed us to determine the processes that led to the pressurization of the conduit and triggering of this large Vulcanian event. Two weeks prior to the 14 July event, daily seismic counts and radial tilt began to steadily increase, indicating the probable intrusion of a new batch of magma into the edifice. The 14 July explosion produced three different juvenile products that were each sampled for this study: airfall; juvenile, vesicular, pyroclastic density current material; and dense plug rocks in the form of ballistic ejecta. Feldspar microlite textures and vesicle size distributions were measured, and used jointly with a two-step recompression model to characterize the spatial distribution of gas in the conduit and the decompression histories of the erupted samples. Model results reveal a vertically stratified conduit with regards to porosity, crystallinity and volatile content prior to the explosion. Overall, our data suggests a complex sequence of events that led eventually to this powerful explosion. 1) Remnants of magma from the previous eruptive phase in May stalled in the shallow conduit, triggering crystallization which, coupled with efficient outgassing, formed a dense (< 2% porosity), highly crystalline plug. This plug had a very low matrix permeability (10^{-17} to 10^{-18} m^2) and high tensile strength (9 to 13 MPa), forming an efficient rigid seal and preventing significant outgassing from the conduit. 2) Just below the plug, a high porosity zone (up to 50%) formed, acting as a gas storage zone, with pressurization occurring partly under closed-system degassing. 3) The shallow conduit became pressurized due to the combination of both gas accumulation and the resistance of the plug to magma column extrusion in response to a new influx of magma. 4) On the 14th of July a critical gas over-pressure was reached, overcoming the strength of the dense plug of magma, trigging extreme decompression and evacuation of the top two kilometres of the conduit. 5) The newly intruded magma was not directly involved in the explosion and continued to ascend during the week following the explosion.

© 2019 Elsevier B.V. All rights reserved.

1. Introduction

During the last 17 year eruptive period (1999–2016), activity at Tungurahua volcano, located 140 km south of Ecuador's capital city of Quito, has varied from relatively benign gas and ash venting and Strombolian outbursts to large Vulcanian and rare but powerful sub-Plinian paroxysmal events (Battaglia et al., 2019; Eychenne et al., 2012; Hall et al., 2015). During the latter part of this eruptive period,

between 2010 and 2016, a new pattern of activity was observed, particularly during eruptive phases in May 2010, December 2012, July 2013, February 2014 and February 2016. These phases were different as they all showed rapid onsets characterized by powerful explosive events following two to three months of relative quiescence and ending with several weeks of low-explosivity Strombolian activity and ash venting (Hidalgo et al., 2015). The paroxysmal Vulcanian events were all characterized by powerful but short-lived explosions, generating ash columns up to 9 km above the crater and pyroclastic density currents (PDCs) that reach populated areas >7 km away from the summit, especially on the northern and western flanks (Hall et al., 2015; Romero et al., 2017).

The initial explosions emitted some of the highest infrasound intensities ever recorded either in Ecuador or at volcanoes worldwide (Anderson et al., 2018), and audible booms that shook the ground and infrastructure, sometimes as far away as the town of Ambato (33 km northwest of Tungurahua). Understanding the processes driving such eruptive dynamics is critical during the onset of Vulcanian explosions which so commonly occur not only at Tungurahua, but also at many andesitic-dacitic stratovolcanoes worldwide, as the reaction time for both the observatory team and community decision makers is very short. Equally, geophysical precursors before Vulcanian explosions are often very subtle. We therefore need to better understand how the processes behind this type of explosion manifest in geophysical data to be able to better interpret any future potential geophysical precursors.

It is generally accepted that Vulcanian explosions occur due to the build-up of pressure below a plug of dense magma that is effectively impermeable to gas flow (e.g. Burgisser et al., 2010; Morrissey and Mastin, 2000; Stix et al., 1997). The amount of pressure that accumulates before a Vulcanian explosion dictates its intensity, and thus how hazardous the explosion might be to the local population. We know that the properties of magma ascending in the conduit are dramatically altered at shallow levels by processes that include the exsolution of magmatic volatiles (Eichelberger et al., 1986; Jaupart, 1998; Stix et al., 1997) and the nucleation and growth of crystals, particularly microlites (e.g. Melnik and Sparks, 1999; Sparks, 1997). The amount of crystals that grow or nucleate is controlled by the rate of ascent and decompression of the magma (e.g. Hammer et al., 2000; Hammer and Rutherford, 2002). The different populations of crystals present in the ejecta therefore record the decompression history of the magma in the conduit. Also, at shallow depth, the permeable outgassing of magma prevents vesicle growth, and promotes vesicle collapse and the densification of magma (Clarke et al., 2007; Diller et al., 2006; Hammer et al., 1999; Heap et al., 2015). This combination of processes results in the formation of a dense, crystalline plug in the shallow part of the conduit. Gas loss or gas retention, and therefore pressurization within the volcanic conduit, are governed by the effectiveness of gas transport mechanisms, which are influenced by the permeable porous network within the magma and conduit walls (e.g. Eichelberger et al., 1986; Gaunt et al., 2014; Klug and Cashman, 1996; Woods and Koyaguchi, 1994). Once gas starts to accumulate, the strength of the plug dictates the maximum pressure that can be built up (e.g. Burgisser et al., 2010; Wright et al., 2006).

Here we apply a multidisciplinary approach to determine the conduit conditions before the 14 July 2013 Vulcanian explosion at Tungurahua, with the aim of understanding what triggered this violent explosion. We use experimental techniques to measure rock permeability and tensile strength, which we combine with a detailed examination of the rock texture and petrology to reconstruct the series of physical states that affected the magmatic system before the explosion by applying a two-step recompression model developed by Burgisser et al. (2010). Geophysical monitoring data, such as deformation, infrasound, seismicity and the measurement of SO_2 emissions, were all integrated into this physical reconstruction to broaden the interpretative context of the experimental and petrological data.

2. 14 July 2013 Vulcanian event

Tungurahua is a 5023 m high stratovolcano located in the Eastern Cordillera of the Andes of central Ecuador, around 140 km south of Quito (Fig. 1). Tungurahua is renowned for its extreme relief (approx. 3200 m above local topography) and extremely steep flanks (up to 40°). On 14 July 2013, after two months of quiescence, an unusually large Vulcanian explosion occurred at 06 h46 (local time = UTC − 5 h), producing an eruption column that rose up to 8.8 km above the crater level and left a millimetre-thick fallout deposit to the west of the vent (Parra et al., 2016). PDCs were generated immediately after the first explosion and traversed the river valleys of Achupashal (runout 7.5 km) and Juive (runout 6.7 km) on the northwest and northern flanks

of the volcano (Fig. 1) respectively (Hall et al., 2015). Additionally, ballistic ejecta produced numerous impact craters on the northern flank of the volcano. One volcanic bomb with an initial diameter of >0.5 m landed approx. 4.3 km north of the vent on the slopes above the community of Pondoa (Fig. 1) creating a 5.1 m diameter and 1.4 m deep impact crater. The first explosion was followed by ~ 2 h of tremor and generated a moderately high column of ~5 km above the crater. Tephra emissions and fallout continued through July with a second, but lesser, peak of activity between the 20th and 24th July, and eruptive activity finally ceased at the beginning of August.

2.1. Geophysical data

In Fig. 2 we plot the radial tilt and the seismic count rate (total number of recorded seismic events per day) recorded at RETU monitoring station and SO_2 output during the period from 1 May to 31 August 2013. RETU monitoring station is located ~2 km to the N of central vent as shown in Fig. 1. A quiescent period lasting around six weeks, from 18 May to 25 June was interrupted by a period of increased tilt around two weeks before the eruption (Fig. 2). SO_2 gas emissions remained at background levels of <400 t/day (as measured by four permanent, automated NOVAC version 1 DOAS monitoring instruments) in the 8 weeks before the eruption (Hidalgo et al., 2015). The explosive event was preceded by an increase in the number of long period (LP) seismic events, which merged to form a continuous tremor signal immediately prior to the eruption (Bell et al., 2018). The first explosion, considered the vent opening pulse, generated a shockwave, recorded by the infrasound network, with a mean acoustic reduced pressure amplitude of 5327 Pa (Hall et al., 2015), while the seismic energy released was approx.1.9×10^9 J (Hall et al., 2015). Both seismic and acoustic energies associated with this explosion were some of the largest recorded since broadband and infrasound monitoring began at Tungurahua in 2006. The continuous seismic tremor continued throughout the eruption and for several hours after the paroxysmal event. This was followed by episodes of sporadic tremor leading to a second moderate explosion at 15 h40 (local time) on the same day. During the explosive phase, SO_2 gas emissions reached over 3500 t/day and remained elevated (> 500 t/day) during the following two weeks (Hidalgo et al., 2015). Inflation signals continued to increase and 700 LP seismic events were recorded during the week after the explosive event, which have been interpreted as due to a continued ascent of magma through the system and outgassing of exsolved gases. Unusually, the tilt signal associated with the renewed intrusion of magma did not deviate from its trend nor show any change associated with the explosions (Fig. 2).

3. Experimental and analytical methods

3.1. Sample material

Samples were collected from four different sites around the volcano (Fig. 1) following the eruptive event. Samples from the three main juvenile product groups, airfall, juvenile vesicular PDC clasts and ballistic ejecta were collected. Juvenile vesicular material was collected from the PDC deposit in the Juive river valleys on the northwest flank of the volcano (Fig. 1). Airfall clasts were collected from a 4×4 m² section of roof in the community of Bilbao which is located around 6 km from the summit on the northwest flank (Fig. 1). These clasts comprise both dense and vesicular material. Samples of dense plug rock material erupted as ballistic ejecta were also collected from the flanks of the volcano after the eruption sequence ended. Large (> 30 cm) blocks were collected from an impact crater at around 4 km from the summit in the farmland above the community of Pondoa (the impact was reported by local farmers) and a second block was collected near the monitoring station RETU, approx. 2 km from the summit on the NE flank, several months after the eruption ended, as soon as it became safe to ascend high on to the volcano's flanks (Fig. 1).
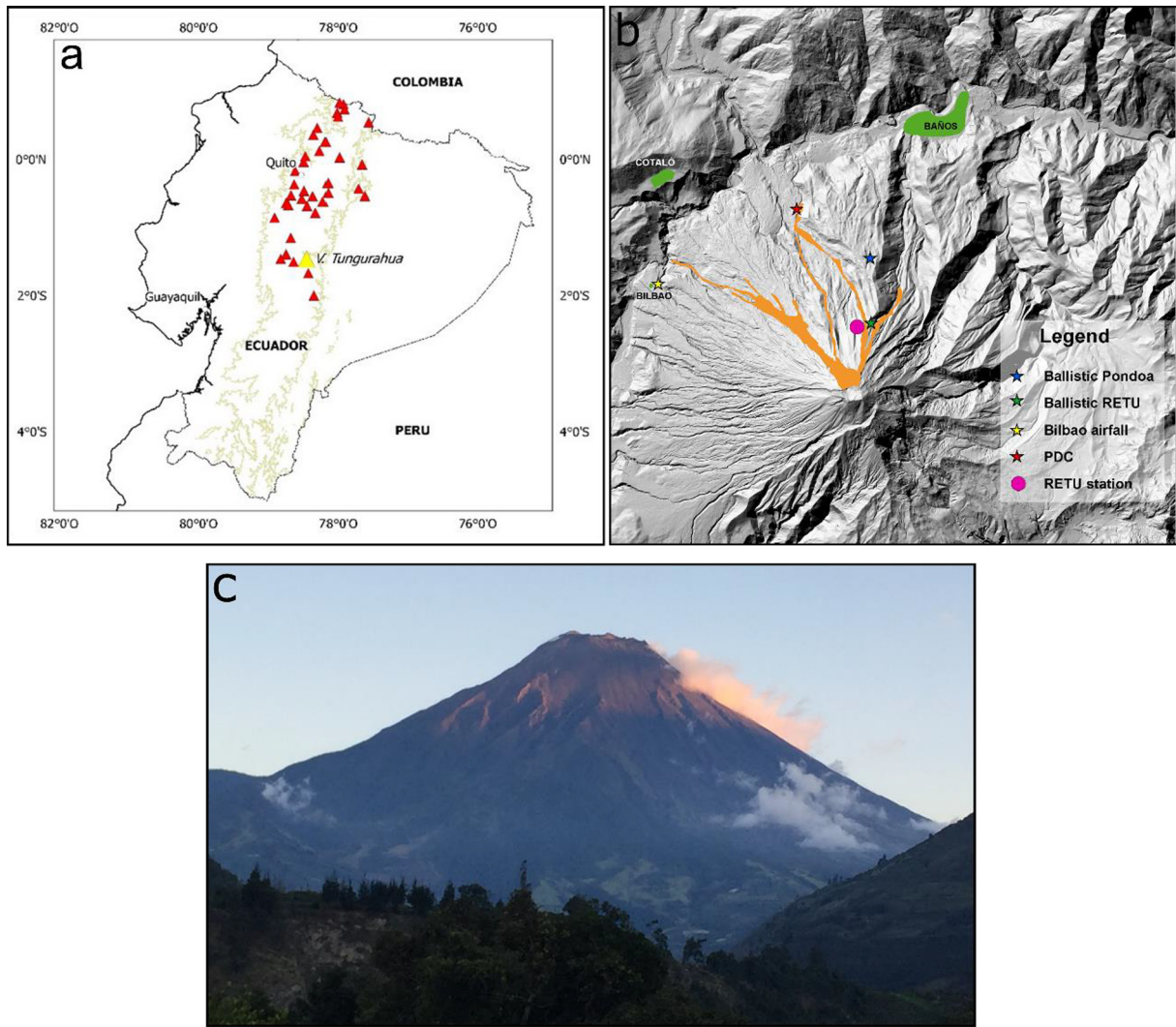
Fig. 1. (a) Location map of Tungurahua volcano, (b) Location map of samples collection sites (stars), RETU monitoring station (pink circle) and the PDC deposits (Orange) (modified from Hall et al., 2015), (c) photograph of Tungurahua volcano looking south. (For interpretation of the references to color in this figure legend, the reader is referred to the web version of this article.)
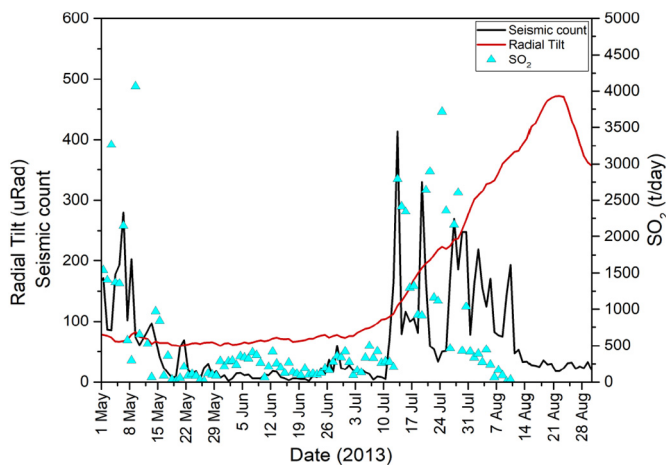

Fig. 2. Geophysical monitoring data. Daily seismic counts (total number of recorded seismic events per day, black line), radial tilt (red line) and SO2 (permanent DOAS measurements, blue triangles) from the 01/05/2013 to 31/08/2013. (For interpretation of the references to color in this figure legend, the reader is referred to the web version of this article.)

3.2. Analytical methods

3.2.1. Textural and petrological analysis

The petrological and textural analysis of the samples was carried out according to the procedures outlined in Burgisser et al. (2010). In brief, polished sections were imaged by scanning electron microscopy (SEM) with a Tescan Vega microscope operating at 15 kV acceleration voltage (DEMEX, Escuela Politecnica Nacional). At least five backscatter electron images (BSE) per sample were taken, one at low magnification (x100) and four at a selected high magnification (at x500, x800, x1000, x1500 and x2000 respectively depending on the average size of the crystals), in order to minimize errors during the textural analysis. Twenty-seven samples were characterized from the three different eruptive product groups. The images were used to quantify the proportions of vesicles, glass, phenocrysts and microlite phases in the samples by manually tracing each of the elements. Manual tracing was used because the low contrast in the grey scale between plagioclase and glass in the BSE images prevented automatic thresholding. The traced images were then converted to binary images, and subsequently, ImageJ software was used to measure the proportions of phenocrysts, microlite and vesicles and the area of glass following the methods of Hammer et al., (2000). The glass proportion is given on a bubble free basis and the

microlite contents are given with respect to the groundmass. The bulk composition of samples of volcanic ash collected during the explosion was also measured using x-ray fluorescence.

3.2.2. Plagioclase groundmass textural characterization

Plagioclase microlites within the groundmass were identified and visually inspected in the high-magnification images from each sample and traced out manually to create binary images. Using these binary images, the area occupied by plagioclase crystals, crystal number and the mean crystal area was quantified. The output of the image analysis was then used to calculate the area fraction (ϕ) and area number density (N_A, the number of crystals per unit area in mm^2) of plagioclase microlites on a vesicle- and phenocryst-free basis (Hammer et al., 2000). The reference area is defined as the phenocryst- and vesicle-free area in the sample. The area number density was calculated by dividing the number of whole crystals by the reference area (Hammer et al., 2000).

3.3. Pre-explosion recompression modelling

The glass proportion and the microlite content of each sample were converted into pre-explosion porosities and pressures using a two stage model that describes the state of the magma just before the explosive event and once the magma has quenched. The model is described in detail in Burgisser et al. (2010). Briefly, this model assumes that the magma was stored in the conduit just prior to the explosion as a mixture of melt, crystals, and pre-explosive bubbles caused by the degassing from the reservoir to the conduit storage level. Bubbles are assumed to contain only water and to be in equilibrium with the melt. During the explosion, new water bubbles nucleate in response to the associated sudden decompression and form two syn-explosive populations: one that is composed of small, isolated bubbles and another that is composed of bubbles that had more time to grow and coalesce. The existing, pre-explosive bubble population also reacts to the explosion by growth and coalescence, which yields a population of large, deformed bubbles. The respective volume proportions of these three populations (isolated syn-explosive vesicles, connected syn-explosive vesicles and connected pre-explosive vesicles, are assumed to be given by the textural analysis (Giachetti et al., 2010). A fraction of the gas imprisoned in the bubbles is liberated (outgassed) during the explosion to propel the ejecta. This fraction can only loosely be constrained by independent observations and is thus a free parameter in the model. The thermal and pressure histories of the ejected clasts when quenched, are recorded in textural characteristics of the samples. Since these histories can rarely be reconstructed, the model uses an estimate of the maximum, near-instant pressure drop that clasts can sustain before breaking as a proxy for quench pressure. This proxy is modulated by a multiplicative factor that is assumed to lie between 0.5 and 2, with a typical value of 1. The upper limits of the quench pressure factor and the outgassing proportion are chosen so that 1) the maximum total water content of every clast lies below a capping value and 2) that all clasts underwent syn-explosive inflation to match textural observations. Following Clarke et al. (2007), the plagioclase microlite contents were used to calculate the pre-explosion pressure through a power law relationship between the feldspar microlite volume proportion of the ground mass and experimental decompression data on microlite crystallization (Andújar et al., 2017; Shea and Hammer, 2013).

3.3.1. Relating plagioclase content to pressure

Microlite contents can be related to pre-explosive magma pressures through decompression experiments and comparisons of natural and experimental microlite contents at suitable quenching pressures. The pre-eruptive conditions of the 2006 Tungurahua eruption were recently determined by Andújar et al. (2017). They performed phase equilibria experiments that suggest magma is stored shallowly at 200 MPa, 975 °C, and under fluid-saturated but water-undersaturated conditions

with 80 mol% H_2O in the fluid phase. The lowest pressure explored in their work was 100 MPa, which is too large to be used to interpret our microlite contents. Experiments by Shea and Hammer (2013), on the other hand, explore the consequences of decompressing a water-saturated basaltic andesite of a composition very similar to both the 2006 (Andújar et al., 2017) and 2013 (this study) magma compositions from Tungurahua (Table 1) at pressures from 150 MPa to 10 MPa at 1025 °C. As both the temperature and water contents are higher than those at Tungurahua, we propose a way to adjust the Shea and Hammer (2013) decompression data to the conditions prevailing at Tungurahua.

The most important control on microlite crystallization during experimental decompression is whether the final pressure is reached in a single step, or following a continuous decompression rate. Single-step decompression produces a larger abundance of microlites at the initiation of the decompression compared to continuous decompression. This larger abundance is due to the large instant undercooling associated with single-step decompression (Mollo and Hammer, 2017). As pressure decreases, the degree of undercooling of both decompression styles become similar, and both eventually reach the same microlite contents at the final pressure. As a result, the modal abundance of microlites as a function of pressure more closely resembles a linear trend in single-step decompression compared to the power-law trend characteristic of continuous decompression (Clarke et al., 2007). It is thus possible to constrain a continuous decompression path by using the starting and ending microlite contents of single-step decompression data. Fig. 3 shows the plagioclase content of the single-step decompression series of Shea and Hammer (2013) alongside 4 runs by rhyoliteMELTS (v. 1.2, Gualda et al., 2012; Ghiorso and Gualda, 2015) representing combinations of the Shea and Hammer (2013) and Andújar et al. (2017) compositions and temperatures. Fig. 3 shows that rhyoliteMELTS underestimates plagioclase contents at 1025 °C, suggesting that a moderate correction to the Shea and Hammer (2013) data is necessary.

Fig. 4a shows the liquidus lines of selected minerals established by Shea and Hammer (2013), Andújar et al. (2017), and rhyoliteMELTS for the Tungurahua conditions (Table 1) with 5 wt% melt H_2O and 1 wt% melt CO_2 at 200 MPa. Our adjustment is based on the assumption that the plagioclase liquidus can be extrapolated from the high pressure constraints given by the Andújar et al. (2017) data to low pressure thanks to rhyoliteMELTS outputs (red vs. green curve in Fig. 4a). The shape of the Shea and Hammer (2013) plagioclase liquidus guides this extrapolation because differences in bulk composition and volatile contents have a minor effect on the liquidus trends (Fig. 3). This adjustment corresponds to shift the Shea and Hammer (2013) liquidus by 35 °C (Fig. 4b). The decompression data acquired at 1025 °C under pure water saturation with the Shea and Hammer (2013) composition can thus approximate the decompression at 990 °C of the Tungurahua

Table 1
Chemical compositions (wt%) of the starting materials used in the studies of Shea and Hammer (2013) and Andújar et al. (2017) and from the bulk composition analysis of ash from the 14 July 2013 explosion.

Oxide	Mascota[a]	Tungurahua 2006[b]	Tungurahua 14 July 2013[c]
SiO_2	58.78	58.51	58.58
TiO_2	0.87	0.89	0.85
Al_2O_3	18.66	16.74	16.33
FeO*	5.6	6.84	7.07
MnO	0.11	0.15	0.08
MgO	3.32	4.18	4.51
CaO	6.77	7.2	6.73
Na_2O	4.08	3.53	3.83
K_2O	1.51	1.76	1.71
P_2O_5	0.3	0.21	0.22

[a] Fused groundmass composition from Shea and Hammer (2013).
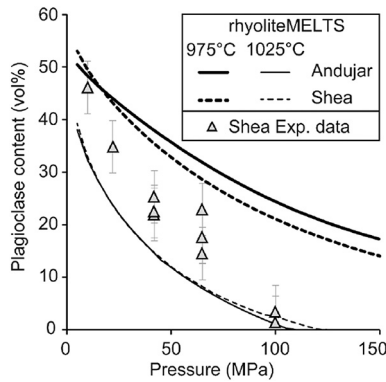[b] Andújar et al. (2017).
[c] Bulk ash sample.

Fig. 3. Plagioclase content as a function of pressure. Triangles are the single-step decompression experiments of Shea and Hammer (2013). Curves are rhyoliteMELT runs with the bulk composition of either Andújar et al. (2017, 6 wt% melt H_2O and no CO_2 at 200 MPa) or Shea and Hammer (2013, 6 wt% melt H_2O and 1 wt% melt CO_2 at 200 MPa) at either 975 °C or 1025 °C.

magma under mixed H_2O–CO_2 saturated conditions. The uncertainty linked to this approximation is on the order of ±10 °C at a given pressure (Fig. 4b). The final extrapolation from 990 °C to the pre-eruptive temperature of 975 °C can be done by shifting all data points along their respective plagioclase isotherms (Fig. 4c). Pure cooling produces mineral phases in proportions that differ from pure decompression (Shea and Hammer, 2013). We expect that large shifts along the isotherm would be affected by such a difference. We however argue that the uncertainty introduced by the modest additional shift we apply here, 15 °C, is likely to be below the 5 vol% uncertainty on mineral proportions reported by Shea and Hammer (2013). The decompression style (single step vs. continuous) causes a level of uncertainty greater than that of adjusting the data of Shea and Hammer (2013) to fit Tungurahua (see Section 3.3). This is why our modelling will consider both decompression styles as end-member scenarios to relate plagioclase microlite content to pressure.

3.4. Experimental methods

3.4.1. Permeability

We performed steady-state flow permeability measurements on samples from two different ballistically ejected blocks of dense andesite plug rock at room temperature and varying effective pressures from 5 to 80 MPa. The effective pressure (P_{eff}) comprises a varying confining pressure (P_c) of 10 to 85 MPa and a constant pore fluid pressure (P_p) of 5 MPa; the simple effective pressure can be calculated as $P_{eff} = P_c - \alpha P_p$ where the poroelastic constant α is assumed to be 1. Permeability measurements were made using a high pressure hydrostatic permeameter designed and built at University College London and described in Benson et al. (2003). The permeameter comprises a pressure vessel pressurized with silicon oil and fed by a nitrogen driven pump; it has a working pressure limit of 280 MPa. Two volumometers supply the pore fluid (pressurized water) at a constant set pressure to each end of the sample which ensures a constant mean pore pressure across the sample.

Cylindrical test specimens measuring 20 mm in diameter were cored from the two blocks and cut to 20 mm in length (with the ends ground flat and parallel with a precision of 0.01 mm). Prior to testing, each specimen was saturated with water under vacuum and then sealed between platens inside a rubber jacket. The specimen assembly was then placed inside the pressure vessel. To conduct a measurement, first a confining pressure was applied, followed by the pore fluid pressure. The system was then left to equilibrate. Once the system was equilibrated, permeability measurements were made by applying a small differential pore fluid pressure of 0.50 MPa across the sample while maintaining the mean pore fluid pressure constant at 5 MPa. Initially the flow rate is
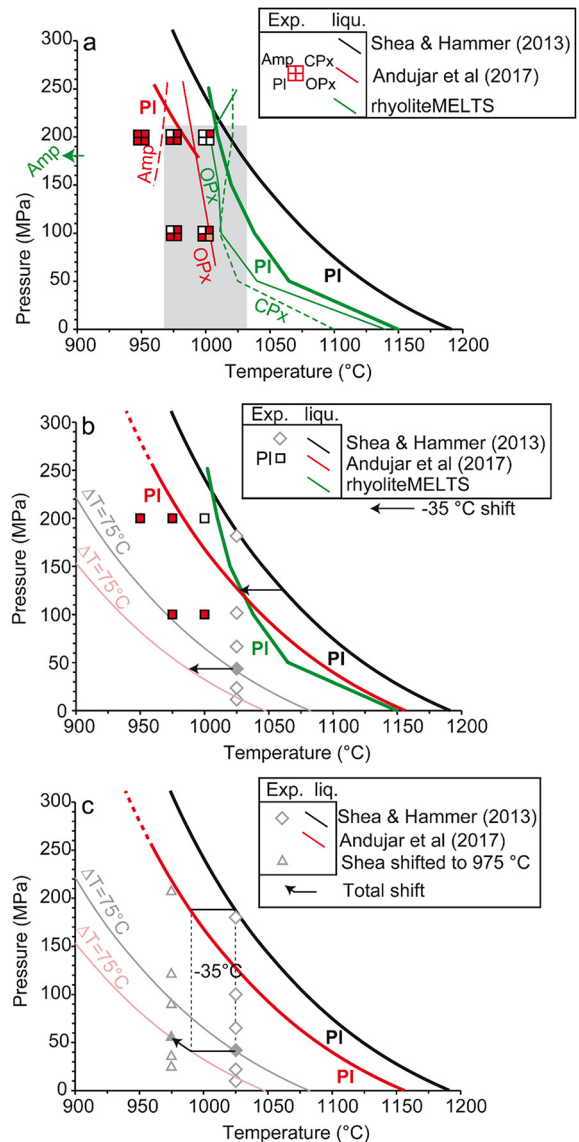

Fig. 4. Phase equilibria diagrams for basaltic-andesite magma compositions relevant for Tungurahua. Black curves are the plagioclase liquidus lines of the basaltic-andesite, at pure water saturation, of Shea and Hammer (2013). Diamonds represent single-step decompressions experiments done by Shea and Hammer (2013). Red curves are the liquidus of selected mineral phases of the Tungurahua magma at 80 mol% of H_2O in the fluid phase. They are based on the squares that represent phase equilibrium experiment of Andújar et al. (2017). Pl, CPx, OPx, and Amp. are plagioclase, clinopyroxene, orthopyroxene, and amphibole, respectively. Squares are filled by red, pink, and white if the corresponding mineral was present, in traces, or absent, respectively. Green curves are liquidus lines of selected minerals from rhyoliteMELTS runs with the Andular et al. (2017) composition. Undercooling isotherms with respect to plagioclase are represented in thin grey and light red lines. a) The grey area covers the P–T domain relevant for our study. The amphibole stability field (green arrow) predicted by rhyoliteMELTS lies outside the axes of the graph. b) Interpolation of the plagioclase liquidus (red line) from rhyoliteMELTS and Andújar et al. (2017) data. For clarity, only plagioclase liquidus lines are shown here and the grey diamond is an illustrative decompression experiment with an undercooling of 75 °C. Horizontal arrows represent a 35 °C shift of the liquidus and undercooling curves between pure water and mixed H_2O–CO_2 experiments (see text). c) Triangles represent the shifted positions of the single-step decompressions of Shea and Hammer (2013). The shift is done by a cooling of 35 °C followed by a translation along the isotherm until the desired temperature of 975 °C is reached (e.g., the arrow linking the filled square to the filled triangle). (For interpretation of the references to color in this figure legend, the reader is referred to the web version of this article.)

transient, but then reaches steady state after a time interval that depends on the sample permeability. Once steady state flow is achieved, permeability can be calculated from the flow rate and the sample dimensions by direct application of Darcy's law. Experimental errors for

the permeability measurements were calculated to be less than ±4% for all samples.

3.4.2. Tensile strength

Indirect tensile strength measurements of samples from the two ballistically ejected dense andesite plug rock were performed using the Brazil test method (ISRM, 1978). The test consists of applying diametral compression to induce tensile stresses in a thin disc of rock. Disc shaped samples either 31 or 25 mm in diameter were cored from the field samples and their surfaces precision ground (with a precision of 0.01 mm) to either 16 or 12 mm in thickness respectively. Sample dimensions and porosity were measured and the samples were then wrapped in masking tape. The samples were placed in the Brazil test jig inside a uniaxial press. The experiments were run at a constant deformation rate of 0.2 mm/min resulting in a test durations of approx. 100 s.

4. Results

4.1. Sample texture and petrology

The samples of dense ballistic ejecta are large blocks, > 30 cm, which shattered into pieces during impact on the flanks of the volcano. Samples are dark grey and massive, with a vitreous appearance and angular fracture surfaces but no obvious fabric. Macro- and micro-fractures are both present in the samples, partially due to cooling and partially due to the impact with the ground. The juvenile vesicular PDC samples are mostly dark grey to black with variable vesicularities and a vitreous lustre but with some oxidation. The airfall clasts contain both dark grey dense clasts and black vesicular clasts with some linear banding in hand specimen in the vesicular clast. Petrological and textural characteristics of the different samples are listed in Table 2. The petrology of all samples is fairly uniform overall with a mineral assemblage comprising plagioclase, clinopyroxene, orthopyroxene and Fe—Ti oxides. The bulk chemical compositions of erupted magma is reported in Table 1.

The results show the magma to be a low silica andesite with 58.5% SiO_2, extremely similar in composition to those reported by Andújar et al. (2017) for the 2006 eruption products. Fig. 5 shows representative SEM backscatter images of the three different groups of eruptive products. The phenocryst content, on a bubble-free basis, varies between the three eruptive product types. The proportion of plagioclase phenocrysts in the dense ballistic ejecta is the highest with an average of 27%, while the PDC juvenile vesicular clasts generally contain the smallest proportions with an average of 22%. The two airfall clasts contain the largest range of proportions with the dense sample containing 32% and the vesicular sample containing 9% plagioclase phenocrysts. All three eruptive products have relatively low clinopyroxene + orthopyroxene content that ranges between 0 and 13%. Texturally, the most marked difference between the eruptive products is in porosity, with the dense ballistic ejecta having between 0.5 and 2% porosity, the PDC juvenile vesicular clasts having between 23 and 66%, and the air fall clasts having a porosity ranging from 2 to 44%. Interstitial glass proportions also vary significantly between and within the dense and PDC juvenile vesicular clasts; from 29 to 37% in the dense ballistic ejecta, and from 16 to 57% in the PDC juvenile vesicular clasts. Despite varying significantly texturally, glass proportions are almost identical between the two airfall clasts (26% in the dense clast and 25% in the vesicular clast). Texturally and petrologically, the dense airfall clast is very similar to the dense ballistic ejecta while the vesicular airfall clasts share properties similar to both the dense and PDC juvenile vesicular clasts.

4.2. Groundmass feldspar textures

The 27 samples analysed showed only a small variety of plagioclase microlite crystal habits ranging from rectangular prisms to acicular crystals. Visual inspection of the plagioclase microlites in the dense plug rock samples yielded mainly tabular crystal morphologies whereas the PDC juvenile vesicular clasts contain occasional swallow-tail and hopper morphologies. Variations in crystal size and population density

Table 2
Petrological and textural characteristics and plagioclase microlite textural characteristics. Phenocryst and glass percentages are given on a bubble free basis. The number density is the number of plagioclase microlite crystals per unit area and the area fraction of plagioclase microlite is given on a vesicle- and phenocryst-free basis. OPX is orthopyroxene and CPX is clinopyroxene.

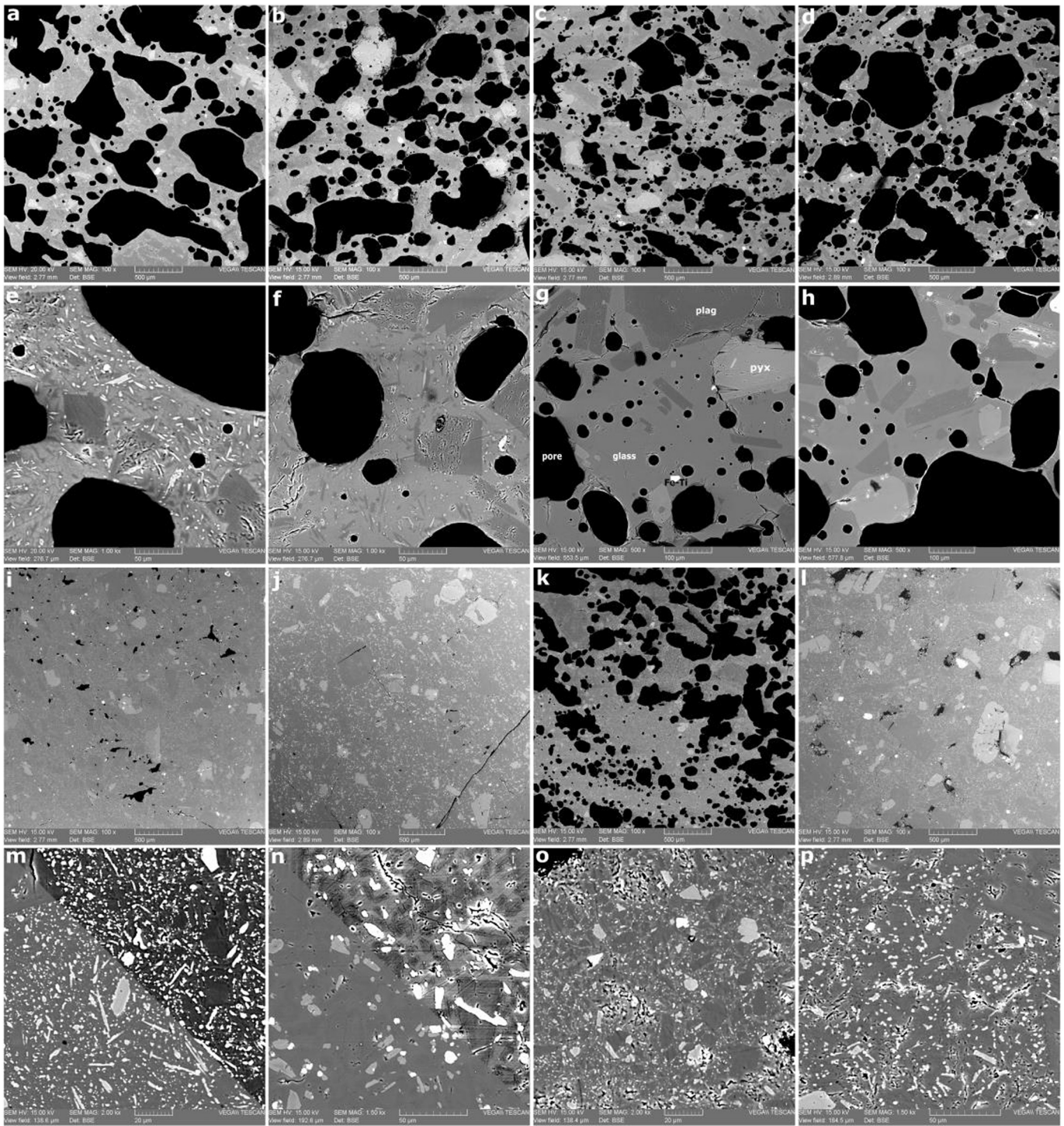| Lithology	Sample number	Vesicle area (%)	Glass area (%)	Plagioclase phenocryst (%)	OPX + CPX phenocryst (%)	Plagioclase microlite 2D areal measurements		
						Area fraction	Number density (mm^{-2})	Mean Crystal Area (μm^2)
Airfall	1	44.3	25.7	9.2	2.2	0.34	33,447	9.55
	2	2.1	26.5	32.2	12.3	0.41	28,207	9.90
Dense plug	4	0.5	33.0	34.0	6.3	0.33	26,811	9.56
	6	2.0	29.3	27.4	5.7	0.41	69,961	4.22
	7.5	1.3	37.9	20.7	7.4	0.38	8879	26.39
PDC juvenile vesicular	11	39.2	34.4	18.7	6.0	0.20	1063	51.00
	12	46.8	33.4	22.5	9.7	0.04	54	43.70
	13	58.3	22.3	23.2	7.6	0.17	2444	21.62
	14	24.0	57.6	28.7	6.5	0.07	941	21.99
	16	24.7	46.9	25.3	5.5	0.26	5171	24.72
	17	33.9	38.2	28.2	6.4	0.08	202	29.24
	18	45.0	32.0	28.2	4.3	0.07	206	10.74
	20	39.9	39.0	23.0	6.2	0.05	99	44.35
	21	47.7	26.0	21.6	13.1	0.15	2915	16.50
	22	55.5	23.7	20.4	5.2	0.22	7455	18.64
	26	66.5	21.1	19.4	8.6	0.06	62	47.37
	27	45.9	31.7	26.0	6.1	0.10	2822	17.62
	28	49.9	27.9	22.2	4.2	0.17	2461	22.30
	29	59.7	26.3	24.7	4.1	0.07	100	28.75
	30	49.0	30.5	14.1	7.7	0.17	3496	26.25
	34	66.0	16.6	14.5	9.9	0.29	3300	29.03
	35	55.9	16.8	22.7	3.2	0.17	6484	18.45
	36	50.3	27.1	22.5	7.1	0.15	2628	32.22
	38	52.2	27.0	33.9	0.0	0.07	67	44.95
	39	30.7	42.0	20.7	11.0	0.07	94	48.28
	40	55.3	23.3	30.2	5.8	0.12	277	54.81
	41	57.6	29.4	18.4	5.6	0.03	62	66.35

Fig. 5. Scanning Electron Microscope backscatter images. a-d low magnification images (x100) of a selection of PDC juvenile vesicular samples and the corresponding high magnification (e and f, x 1000 and, g and h, x 500). Examples of Plagioclase (plag), pyroxene (pyx), Fe—Ti oxides (Fe—Ti), glass and pores are labelled in g. Low magnification images of the dense ballistic ejecta (i and j at x100) and a vesicular (k, x100) and dense (l. x100) samples of the airfall deposit. m and n are the corresponding high magnification images of the dense ballistic ejecta (x 2000 and x1500 respectively) with an increases level of contrast in the top right section to allow the plagioclase crystals to be distinguished from the glass. o and p are the high magnification images of the vesicular (o, x2000) and the dense (p, x1500) airfall samples.

exist between the three different eruptive product groups (Table 2). The dense plug rock samples have the highest recorded crystal number densities at between 9000 and 70,000 mm^{-2} while the lowest recorded crystal number densities are in the PDC juvenile vesicular clasts at between 50 and 7500 mm^{-2} (Fig. 6a). The airfall clasts (both dense and vesicular), on the other hand, are more similar to the dense products with between 28,000 and 33,500 mm^{-2}, respectively. Within the dense plug rock and airfall clasts (both dense and

vesicular), the feldspar area fraction ranges from 0.32 to 0.41 whereas the PDC juvenile vesicular clasts feature lower values that range between 0.03 and 0.29 (Fig. 6a). This is a function of both the size and the number of crystals, since many small crystals can produce the same crystallinity as a small number of large crystals. The mean crystal area ranges between 4.2 and 26 μm^2 in the dense plug rocks and the airfall clasts but are generally larger in the PDC juvenile vesicular clasts at 10–66 μm^2 (Fig. 6b).
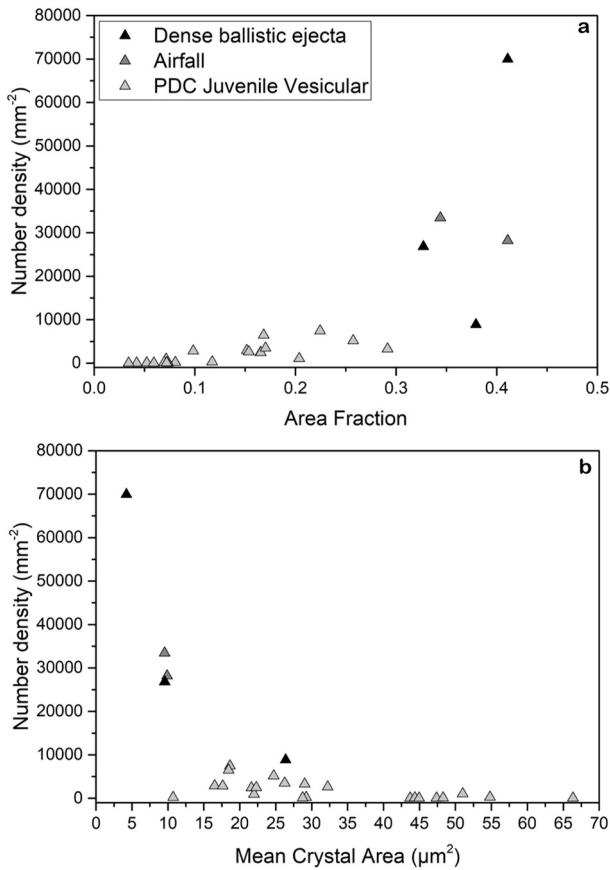
Fig. 6. Batch textural results. (a) Feldspar microlite number density as a function of area fraction and (b) feldspar microlite number density as a function of mean crystal area. Black triangles show the dense ballistic ejecta, mid grey the airfall samples and light grey the PDC juvenile vesicular samples.

4.3. Pre-explosion magma conditions

The plagioclase content of the decompression series of Shea and Hammer (2013) adjusted to Tungurahua conditions (see Section 3.3) is shown in Fig. 7. We added to these data a constraint at low pressure

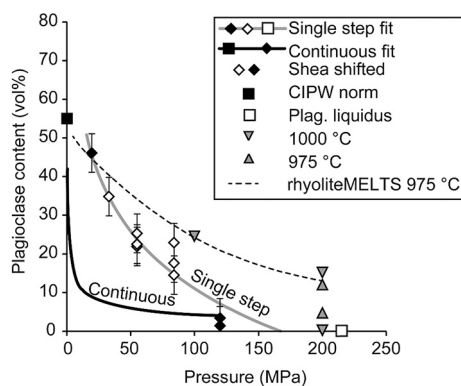**Fig. 7.** Plagioclase content as a function of pressure. Diamonds are shifted data of the decompression runs of Shea and Hammer (2013). The open square is the water-undersaturated plagioclase liquidus of Fig. 4b. The black square is the maximum plagioclase content at 1 bar. The black curve is a power-law fit of the black-filled symbols that represent a slow continuous decompression. The grey curve is a logarithmic fit of the decompression runs, the plagioclase liquidus and the 1 bar data point. Triangles represent phase equilibrium runs from Andújar et al. (2017) and the dashed line is the corresponding rhyoliteMELTS decompression (run "Andujar" at 975 °C of Fig. 3).

by calculating the CIPW norm at 1 bar of the Tungurahua magma bulk composition. The resulting 55 vol% of plagioclase is consistent with the highest contents of plagioclase measured in our samples, which is 54 vol% of microlite plus phenocrysts on a bubble-free basis for a dense plug sample. As expected, these adjusted single-step decompressions produce less plagioclase than both the phase equilibria data and the rhyoliteMELTS run (Figs. 3 and 7). We used the representative fit of these adjusted single step data, one end-member relationship, which yields $pl = -21.36 \ln P + 158.5$, where pl is the plagioclase content in vol% and P is the pressure in bars. The natural magma, however, decompressed in a more continuous manner than the experiments. The 14 July 2013 Vulcanian explosion, likely involved magma that ascended to shallow levels during the May 2013 activity. Microlites thus grew in response to slow (ascent durations longer than weeks) decompression that more closely followed continuous decompression than large and sudden steps in decompression. We thus fitted a power law, $pl = 84.1 P^{-0.428}$, to the lowest and highest pressures of the adjusted data (19.5 and 120 MPa, respectively) to create the other end-member relationship.

Our data show that the plagioclase phenocryst content varies between 9 and 37 vol% (Fig. 8). Interestingly, this variation is correlated with the amount of groundmass, which suggests that equilibrium conditions cover a range of pressure, temperature, and/or water contents. Microlite content, on the other hand, is not correlated with the amount of groundmass. This makes the choice of a baseline impractical for the use of the fits of Fig. 8 as representing bubble-free modal proportions. Instead, we chose to consider that the data of Fig. 8 represent the microlite content with respect to groundmass. The starting conditions (175 MPa in adjusted pressure) are below the plagioclase liquidus (215 MPa) but the experimental charges contain <3 vol% plagioclase, which is less than the 9–37 vol% (Table 3) of the natural products. The natural glass composition was thus more evolved than the experimental one at the beginning of the ascent from the reservoir. Quantifying precisely how this difference affects the microlite proportion is difficult, but the effect is likely to be below the 5 vol% uncertainty associated with mineral proportions determinations.

To estimate pre-explosive pressures and porosities using the two-stage recompression model (Burgisser et al., 2010), a magma temperature of 975 °C and a bubble-free magma density of 2455 kg/m³ (i.e., melt + crystals) is assumed (Andújar et al., 2017). The two free parameters linked to bubble populations were constrained by the proportions of the three vesicle types and their uncertainties. Isolated syn-explosive vesicles, connected syn-explosive vesicles, and connected pre-explosive vesicles are present in respective proportions of 9 ± 11:66 ± 25:25. Following Burgisser et al. (2010), the parameter constraining the amount of overpressure that clasts can sustain was set to a reference value of $1_{-1}^{-0.5}$. The upper and lower values of the last parameter, which quantifies outgassing, were chosen so that the maximum total water content is ≤6 wt% (Andújar et al., 2017) and that all clasts had net syn-explosive inflation, as suggested by textural
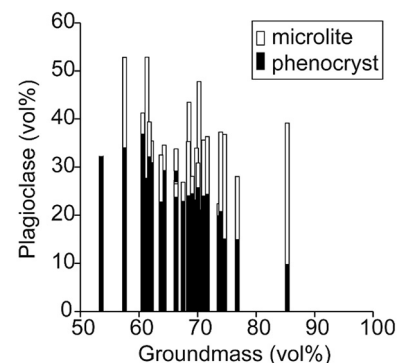

Fig. 8. Plagioclase contents as a function of groundmass on a vesicle-free basis.

Table 3

Textural characteristics and results on the pre-explosive conduit conditions. "Plag μlite" and "Px μlite" indicate the proportions of plagioclase microlite and pyroxene microlite, respectively. "Plag/matrix" is the ratio of plagioclase microlite and groundmass (glass plus microlite). "Syn isol", "Syn conn", and "Pre conn" respectively represent the proportions (to 100%) of syn-explosive and isolated vesicles, syn-explosive and connected vesicles, and pre-explosive and connected vesicles. Depths are measured from the vent down and are considering respectively magma-static (Magma depth) and litho-static (Lith. depth) conduit pressure gradient. Values in parenthesis are one standard deviation.

Sample	Plag μlite (vol%)	Px μlite (vol%)	Glass (vol%)	Syn isol (%)	Syn conn (%)	Pre conn (%)	Plag/matrix (%)	Pressure (MPa)[a]	Porosity (vol%)	Magm. depth (km)	Lith. depth (km)
1	16.5 (2.4)	6 (2.1)	25.4 (2.8)	2.6	60.6	36.8	34.5	0.8 (0.4,0.2)	29.1 (0.9)	0.04	0.03
2	21.5 (2)	4.6 (0.8)	26.3 (1.7)	11.4	87.7	1.0	41.1	0.5 (0.1,0.1)	1.1 (0.1)	0.02	0.02
4	18.7 (2.2)	5.9 (0.6)	32.7 (2.1)	11.7	3.3	85.0	32.7	0.9 (0.3,0.2)	0.27 (0.03)	0.04	0.04
6	24.7 (2.8)	6.4 (0.8)	29 (2.6)	12.5	81.2	6.3	41.1	0.5 (0.2,0.1)	1 (0.3)	0.02	0.02
7.5	26.3 (3.9)	6 (1.6)	37 (3.7)	57.7	24.3	17.9	37.9	0.6 (0.3,0.2)	0.7 (0.1)	0.03	0.03
11	9.3 (1.3)	2.3 (0.5)	34 (1.8)	2.3	97.7	0.0	20.4	2.7 (1.2,0.7)	25 (0.3)	0.16	0.11
12	1.5 (0.7)	1.1 (0.7)	33 (1.2)	6.8	87.7	5.5	4.2	109 (91,63)	1.4 (0.01)	4.79	4.27
13	4.8 (1.8)	2.1 (2.1)	22 (2.7)	2.5	50.9	46.6	16.5	4.5 (8.9,2.4)	30.5 (0.4)	0.26	0.18
14	1.9 (0.7)	1.1 (0.5)	23.7 (1.6)	27.9	39.2	32.9	7.2	31 (68,17)	5.9 (0.2)	1.48	1.23
16	9.5 (1.1)	3.4 (0.8)	23.9 (1.5)	4.5	85.0	10.5	25.8	1.6 (0.5,0.4)	31 (1)	0.09	0.06
17	3.4 (0.7)	1.5 (0.5)	37.8 (1.8)	8.0	83.9	8.1	8.1	24 (16,8)	4.9 (0.1)	1.16	0.94
18	2.5 (0.7)	2.5 (1.1)	31.7 (2)	4.0	58.1	38.0	6.9	34 (41,15)	4.2 (0.1)	1.62	1.35
20	2.2 (0.7)	1 (0.6)	38.7 (1.2)	9.5	72.8	17.7	5.2	66 (20,14)	2.03 (0.04)	2.98	2.59
21	5.1 (1.7)	2.8 (1.9)	25.7 (1.8)	5.9	91.2	2.8	15.3	5.4 (8.1,2.6)	22.6 (0.4)	0.31	0.21
22	7.4 (2.8)	2.4 (1.7)	23.4 (2.7)	2.0	98.0	0.0	22.3	2.2 (4.6,1.2)	39.1 (1)	0.13	0.09
26	1.3 (0.9)	0.9 (0.7)	20.9 (2.5)	7.4	47.3	45.3	5.8	51 (149,36)	4.6 (0.2)	2.35	2.01
27	3.5 (0.7)	1.2 (1.4)	31.4 (2.6)	5.8	70.4	23.8	9.8	15 (10,5)	9.1 (0.3)	0.78	0.60
28	5.9 (2.2)	2.5 (1)	27.6 (3.7)	6.3	53.1	40.5	16.4	4.6 (9.1,2.4)	26.4 (0.8)	0.27	0.18
29	2.1 (0.9)	0.5 (0.2)	26.1 (1.4)	3.6	65.0	31.4	7.3	30 (82,17)	6.4 (0.05)	1.43	1.18
30	6.7 (1.1)	2.6 (1.1)	30.2 (2.1)	7.3	23.4	69.3	17.0	4.2 (2.2,1.2)	28 (0.6)	0.24	0.16
34	7.5 (0.9)	1.9 (0.4)	16.5 (1.6)	2.1	76.5	21.5	29.1	1.2 (0.4,0.3)	49.7 (1.3)	0.06	0.05
35	5.4 (0.7)	2.4 (0.6)	24.2 (2.5)	6.5	85.9	7.6	16.8	4.3 (1.5,1)	30.2 (0.6)	0.25	0.17
36	5.4 (0.6)	2.8 (1.6)	26.9 (1.5)	3.8	89.0	7.2	15.4	5.3 (1.6,1.1)	23.9 (0.2)	0.31	0.21
38	2.1 (0.6)	0.5 (0.3)	26.7 (1.5)	7.5	38.5	54.0	7.2	31 (38,14)	5.3 (0.1)	1.48	1.22
39	3.3 (1.3)	1.3 (0.3)	41.6 (1.1)	15.2	75.2	9.6	7.2	31 (67,17)	3.7 (0.1)	1.46	1.21
40	3.28 (0.02)	1.61 (0.01)	23.1 (0.2)	5.7	47.0	47.3	11.7	10 (0.1,0.1)	15.7 (0.3)	0.54	0.39
41	1.1 (0.3)	1.5 (0.4)	29.1 (1.3)	5.5	87.0	7.4	3.5	174 (26,79)	1.11 (0.02)	7.51	6.81

[a] The first value in parenthesis is the negative error and the second value is the positive error.

observations. The former condition is consistent with a small amount of microlite at the inferred reservoir pressure of 200 MPa (Fig. 7). For consistency, the relationships relating plagioclase microlite content to pre-explosive pressure were clipped to a maximum pressure of 200 MPa. These conditions imply that between 10 and 70% of the gas present within the magma syn-explosively was outgassed (outgassing proportion model parameter). As this free parameter has only a modest effect on pre-explosive porosity, we therefore assumed a reference value of 50% for this poorly constrained parameter.

Fig. 9 shows the pre-explosive values of pressure and porosity for the 27 analysed samples. The input parameters for the recompression model are shown in Table 3. Results suggest a stratified magmatic column with a dense, thin plug of rock near the surface with <2 vol% porosity. The porosity of samples from this region is dominated by microfractures with scarce remnants of vesicles and almost no pre-explosion porosity, which means that the samples did not experience any syn-explosive expansion. The dense plug sits directly above a 600 m thick region of high porosity (20–50 vol%) that contains samples with the largest proportion of large, connected pre-explosive vesicles and only a small proportion of syn-explosive vesicles. Syn-explosive expansion of these samples was modest (a porosity gain of 15 to 30 vol%). Below this high porosity region there is a zone containing a cluster of samples that cover a small range of porosity (3–6 vol%) and depth (~700 to 1500 m). Samples from this zone contain moderate amounts of pre-explosive connected and deformed bubbles. These bubbles, however, are on average smaller and less elongated than in the region above. These samples also experienced the largest syn-explosive expansion (gain of 30 to 60 vol%). Below approx. 1.5 km depth, there are only 4 samples with relatively low pre-explosion porosity that contained connected vesicles of modest size that are not very deformed. The deepest-sourced samples also experienced large syn-explosive expansion (38 to 56 vol%). Overall, the model suggests that the deepest evacuation possible was between 4 and 7 km (although these depths are associated with

the greatest uncertainty) and that all but three samples came from shallower than 2 km.

4.4. Experimental results

In Fig. 10, we plot the results from a series of steady-state permeability measurements on samples of dense andesite from three ballistically ejected field samples. Two samples were intact with no visible fractures
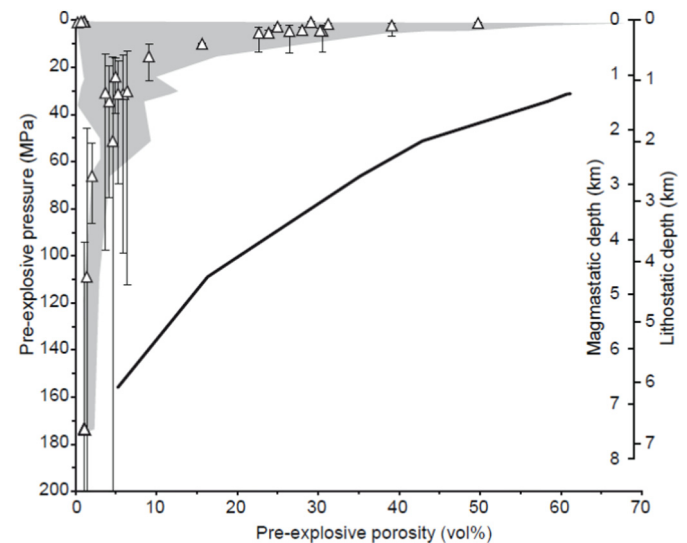

Fig. 9. Pre-explosive conditions represented by porosity as a function of pressure and depth. Triangles indicate the average model outputs for each sample, grey areas cover the ranges of outputs of the 10 parametric model runs, and error bars represent the combined effects of natural variability and analytical uncertainty on each sample. The solid black curve indicates closed-system degassing if the pure water saturation pressure is 200 MPa.
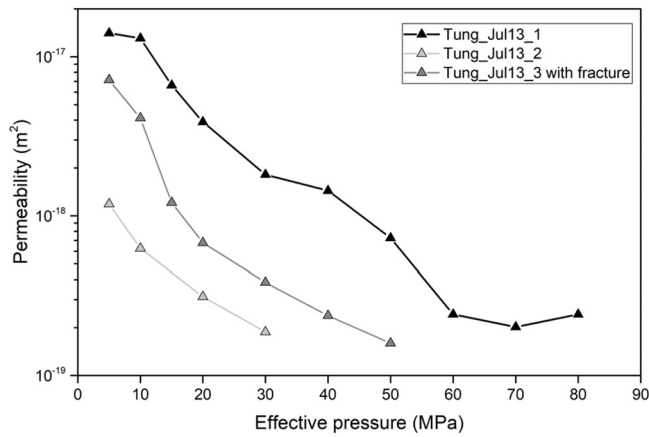
Fig. 10. Permeablity as a function of effective pressure on three samples of dense plug rock. Sample 1 from Pondoa and samples 2 and 3 from RETU. Sample 3 has a visible fracture running axially through the prepared sample.

(Samples 1 and 2) and the third (Sample 3) had a visible macro-fracture running axially through the prepared sample, and hence in the direction of water flow in the experiment. The presence of fractures complicated sample coring. The measured permeability for all three samples was between 10^{-17} and 10^{-18} m^2 at the lowest effective pressure of 5 MPa. These values are at the lower end of published values for crystalline and volcanic rocks. For Sample 1 (collected from Pondoa) the permeability decreased by nearly 2 orders of magnitude, from 1.5×10^{-17} m^2 to 2×10^{-19} m^2, as the effective pressure is increases from 5 to 80 MPa. By contrast, the starting permeability of Sample 2 (collected from RETU) was an order of magnitude lower than the Pondoa sample at 1×10^{-18} m^2, and reduced to 1×10^{-19} m^2 by an effective pressure of only 30 MPa. Unsurprisingly, the sample collected from RETU that contained a through-going macrofracture (Sample 3) exhibited a significantly higher starting permeability (7×10^{-18} m^2) compared with the intact sample from the same location (Sample 2, 1×10^{-18} m^2). Increasing the effective pressure acted to close the macro-fracture in this sample, which resulted in a close to 2 orders of magnitude decrease in permeability to 1×10^{-19} m^2 by an effective pressure of 50 MPa.

Indirect tensile strength tests were conducted on 10 intact samples, 6 from the sample collected in Pondoa and 4 from the ballistic block collected near the RETU monitoring station. The tensile strengths of the samples from the Pondoa block range from 10 to 13 MPa and the tensile strengths of the samples from the RETU block ranged from 9 to 10 MPa.

5. Discussion

5.1. Pre-explosion conduit conditions

Results from a two-step recompression model reveal a vertically stratified pre-explosion conduit at Tungurahua prior to the 14 July 2013 Vulcanian explosion (Fig. 9). The model suggests that an extremely dense but thin plug of degassed magma resided in the shallowest part of the conduit. With such low porosities that are dominated by micro-fractures, there is no evidence for any syn-explosive expansion or volatile exsolution in the plug. Plagioclase microlite number densities are also highest in samples from this zone (up to 70,000 mm^{-2}, Fig. 11). Relatively high number densities usually occurs as a result of moderate undercooling in the rising magma (Hammer et al., 1999; Hammer and Rutherford, 2002) although, the absence of disequilibrium crystal morphologies in these samples suggests only low to moderate decompression rates (Couch et al., 2003). In this case, the long residence times of the magma (>6 weeks since the last eruptive event) indicates that crystal and vesicle textures in the plug samples are more likely the result of the dwell time at low pressure rather than
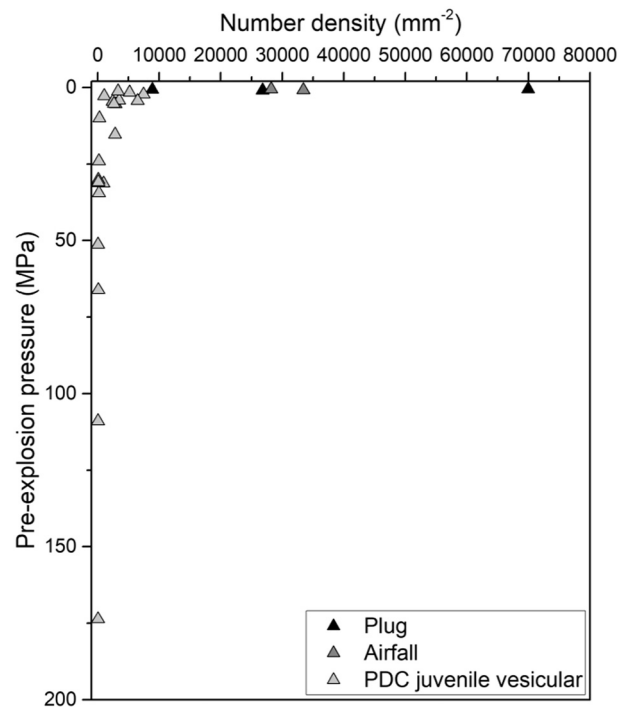

Fig. 11. Plagioclase microlite number density as a function of the sample pre-explosion pressure as calculated by the recompression model.

ascent (Preece et al., 2016). Efficient outgassing under open-system conditions is also suggested by the textural characteristics exhibited by the plug rock samples particularly, their low porosity nature, where almost no vesicles are present, indicating that the densification processes were apparently very efficient. We suggest that the dense samples from the shallowest parts of the conduit, represent the degassed, highly crystallized remnants of magma from the last eruptive phase in May 2013. This magma likely ascended at moderate rates, triggering crystal nucleation and growth during the final part of the last eruptive phase. Stiffening of this magma and the dwindling magma supply caused the magma to stall, and open-system outgassing conditions prevented vesicle expansion and promoted further crystallization and densification of the magma (Clarke et al., 2007; Hammer et al., 1999).

Directly below the dense plug is a high porosity zone (up to 50 vol%) where the magma contains many large connected but deformed vesicles, which indicates that extensive closed-system degassing occurred with only a comparatively insignificant amount of outgassing. The magma experienced only a relatively small amount of syn-explosive expansion (3 to 34%) because it already experienced significant closed-system degassing during ascent and residence in the conduit. Feldspar number densities are substantially reduced in this zone (300 to 7000 mm^{-2}, Fig. 11) when compared with the plug-rock which is consistent with lower undercooling, and therefore with the dominance of crystal growth over nucleation (Hammer et al., 2000; Hammer and Rutherford, 2002; Preece et al., 2016; Shea and Hammer, 2013). This is confirmed by larger mean crystal areas measured in samples from this depth. Nevertheless, disequilibrium crystal morphologies such as swallow tale and Hopper forms are occasionally present in the samples from this intermediate zone. While the majority of crystals are equant and tabular, which suggests modest undercooling during slow decompression, the presence of disequilibrium crystal morphologies resulted from moderately higher degrees of undercooling associated to more rapid decompression, even if only for a short time.

A cluster of the collected samples were evacuated from approx. 1 to 2 km depth, which is consistent with the depth of explosion earthquakes at Tungurahua estimated by Battaglia et al. (2019) and Kim et al. (2014). Crystal number densities continue to decrease

(60–900 mm^{-2}, Fig. 11) with depth which is consistent with a change at greater depth to a crystal growth dominated regime with low undercooling. Mean crystal areas also increase with depth, which supports this progressive change to crystal growth due to low decompression rates. Only three samples correspond to depths > 2 km (Fig. 9) although, the resulting pressures and depths have the largest levels of uncertainty. These samples had the lowest number density of plagioclase microlites (Fig. 11), which suggests the lowest undercooling values (Hammer and Rutherford, 2002). Mean crystal areas are also the largest in these deep samples, which suggests growth-dominated crystallization, often associated with very low ascent rates. However, the textures present in the deepest samples most likely resulted from protracted residence times rather than from decompression. With sudden onset eruptions that occur over minutes, the samples quenched before the melt could reorganize to allow the nucleation of new crystals, which explains the lack of tiny microlite crystals within these samples (Brugger and Hammer, 2010; Couch et al., 2003; Hammer et al., 1999) and suggests rapid syn-explosive ascent. These deep-seated samples, however, still had the time to experience high levels of syn-explosive expansion (>50 vol%) before quenching, as shown by the high percentage of isolated syn-explosive vesicles and the smaller percentage of connected, deformed pre-explosive vesicles compared to the shallower samples.

Fig. 12 shows number density vs area fraction in samples from numerous different eruptions (Fig. 12a) of different size and intensities and also results from decompression experiments on natural samples
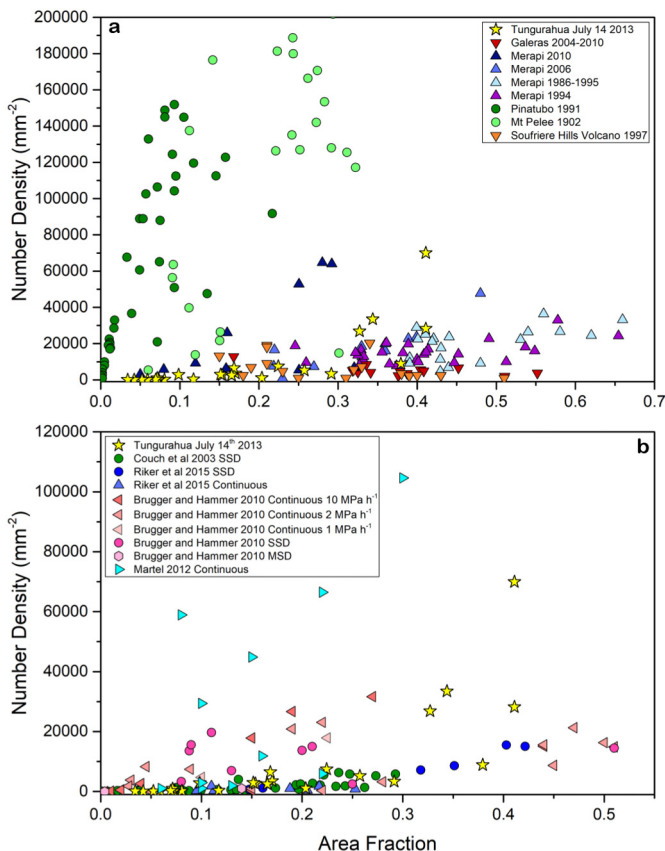

Fig. 12. Microlite area fraction as a function of microlite number density for (a) various eruptions ranging from high intensity Plinian events to low intensity effusive events and lava dome building events. Data from Pinatubo 1991 (Hammer et al., 1999), Mt. Pelee 1902, various eruptions of Merapi 1986–2010 (Preece et al., 2016; Hammer et al., 2000), Galeras 2004–2010 (Bain et al., 2018) and Soufrière Hills Volcano 1997 (Clarke et al., 2007). (b) Experimental decompression data from continuous decompression experiments (Riker et al., 2015; Brugger and Hammer, 2010; Martel, 2012), single step decompression experiments (Riker et al., 2015; Couch et al., 2003; Brugger and Hammer, 2010) and multistep decompression experiments (Brugger and Hammer, 2010).

(Fig. 12b). The position of the Tungurahua samples overall suggests low intensity-eruption comparable to dome forming eruptions (Fig. 12a, yellow stars). The number density in the plug rock samples is, however, somewhat elevated compared to the other low-intensity eruptions. Overall, the crystal number density and area fraction at Tungurahua are comparable to several decompression experiments (Fig. 12b). The highly vesicular samples from the PDC deposits are most comparable to the single-step decompression data by Couch et al. (2003) and to the continuous decompression experiments at 1 and 2 MPa h^{-1} by Brugger and Hammer (2010). However, the number density and area fraction of the plug rocks cannot be explained by any of the published experimental data. The single-step decompression data from Riker et al. (2015) closely approximates the feldspar area fraction of the plug rocks, but underestimates the microlite number density. Continuing the trend of Brugger and Hammer's (2010) continuous decompression data at 10 MPa h^{-1} would match well the plug rock data from Tungurahua. However, no single experimental set can fully describe all of the number density and area fraction data from Tungurahua, which suggests that the feldspar microlite densities and area fractions of the different levels in the conduit were produced by different decompression dynamics. The deeper samples likely underwent slow and potentially continuous decompression and samples from the plug were affected by more rapid or potentially stepwise decompression. Our samples underwent increasing nucleation rates and crystallinity with decreasing quench pressure, but the bulk of our observations suggests only modest ascent rates that are generally linked to low-intensity eruption (Fig. 12a). The scant presence of evidence for higher rates of decompression and more significant undercooling suggests that some crystal textures resulted from ascent and decompression during the end of the May activity. Most textures, however, were generated during the 2-month residence time prior to the July activity.

5.2. Preparing the 14 July event: plug formation

Low-level explosive activity and ash and gas venting concluded the previous eruptive phase at Tungurahua during May 2013 (Hidalgo et al., 2015). Dwindling magma supply probably caused the remnants of the magma from this phase of activity to stall in the shallow conduit, where they continued to outgas (Fig. 13). Seismicity and deformation were both relatively low in the weeks following this period, indicating little to no magma migration. The long (>6 weeks) residence time in the conduit before the 14 July explosive event is expressed in the textual characteristics of the plug rock. Measured SO$_2$ emissions returned rapidly from elevated levels during the May activity to low levels (<100 to 400 t/day) in just a few days (Hidalgo et al., 2015). As the magma stagnated in the conduit, it continued to crystallize and degas in open-system conditions, leading to a vertically stratified density profile with the densest section at the top (Clarke et al., 2007; Diller et al., 2006; Riker et al., 2015). Our results show that the matrix permeability of this dense plug was very low, significantly reducing its ability to transport gas. Our mechanical tests revealed up to 13 MPa tensile strength that is partly due to very low porosities and high crystallinities of these dense samples. We acknowledge that permeability and strength data here represent only the matrix material rather than the plug as a whole, because large-scale features such as fracture zone are larger than the sample size used in the experiments (Heap and Kennedy, 2016). Therefore, our results provide respectively a lower and an upper limit for these two properties. When combined, these properties characterize an efficient plug at the very top of the conduit.

Continued low-level emissions of SO$_2$ recorded in the interim weeks (from the 20 May to the 23 June), despite the low permeability of the matrix material of the plug, suggest that larger permeability pathways such as large fracture networks were bleeding gas out of the system (e.g. Gaunt et al., 2014; Stix et al., 1997), but the flux was not sufficient to prevent gas pressurization. Closed-system degassing within the stalled magma continued and the conduit once again entered a state
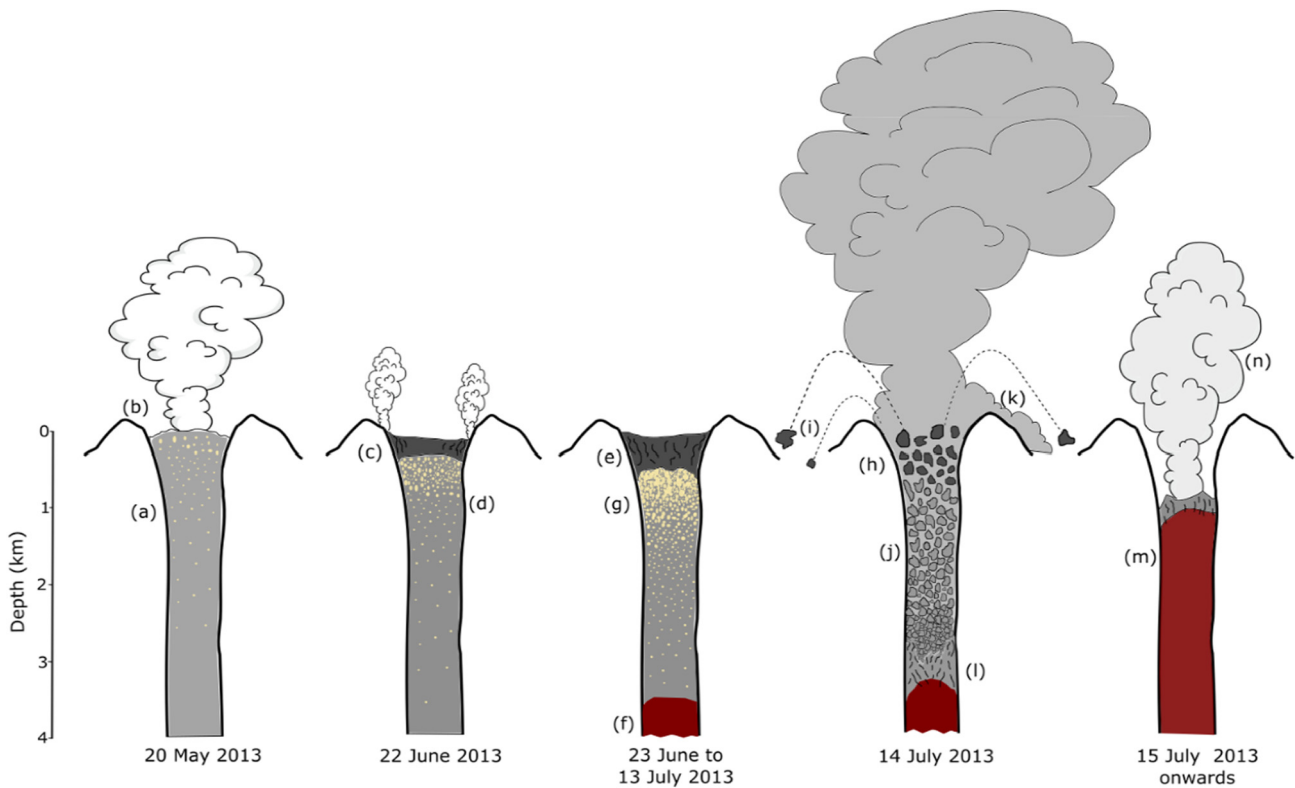
Fig. 13. Sketch showing the processes linked to the 14 July 2013 Vulcanian event. Annotations on the sketches describe the characteristics of each phase. The magma that ascended during the May activity stalled in the conduit (a) due to dwindling supply rate and an increase in magma viscosity while gases freely escaped from the magma column (b). Magma in the conduit continued to degas and crystallize, resulting in densification (c). Closed-system degassing coupled with the formation of an efficient seal atop the conduit (d) began gas over-pressurization. Densification created a highly efficient plug (e) with low permeability and high tensile strength that sealed the conduit to significant gas escape. On 23 June tilt and seismic data indicated the beginning of a new intrusion of magma (f) into the base of the edifice. Volatile exsolution from this new magma fluxed upward, collecting in the high-porosity zone below the plug (g), significantly increasing gas overpressure. On the 14 July, a critical gas-overpressure was reached. It overcame the strength of the plug rock (h), blasting it apart and causing rapid decompression of the magma in the top 2 km of the conduit. The blocks of shattered plug rock were ballistically ejected (i), landing as much as 4 km away from the summit. The decompression caused extensive fragmentation of the magma column (j), generating an eruption column 8.3 km above the crater and pyroclastic density currents (k). The conduit was efficiently evacuated down to ~2 km with only a small proportion of magma potentially evacuated from deeper (l). After the explosion, the new intrusion of magma continued its slow ascent (m), causing low-level explosive activity and ash venting (n) during the following week. The conduit once again began to seal itself while magma continued to ascend, resulting in a second Vulcanian explosion on 18 October 2013.

of modest over-pressurization. The formation of an effective plug and pressurization of the conduit prior to the July event in this instance was therefore likely a gradual process, occurring over a period four to six weeks, similar to what was suggested for the 1992 activity at Galeras volcano, Colombia (Stix et al., 1997).

5.3. Activity leading up to the 14 July event: conduit processes

The start of a new intrusion of magma was first signalled on 23 June by the modest increases in the number of seismic events and in deformation as indicated by increased tilt (Fig. 2). Analysis and modelling of the tilt signal by Neuberg et al. (2018) suggests that the most probable source of the tilt comes from shear stress along the conduit walls generated by the intrusion of magma into the conduit. Although they acknowledge that the 14 July 2013 event is somewhat different from the other events they analysed, their results suggest that the tilt generated during the two weeks before the eruption was indirectly caused by new magma ascending to approx. 3000 m below the summit. Importantly, this is deeper than the quench pressures proposed for the majority of the Tungurahua samples, by the recompression model. Likewise, the tilt data also suggests that the ascent of this new batch of magma continued at the same rate before, during and after the 14 July, undisturbed by the explosion, adding to the evidence that the magma ascent causing the tilt was deeper than the evacuation level of the explosion.

The microlite crystal textures in the samples from Tungurahua suggest low ascent rates and long residence times that are most comparable to those generated by low intensity eruptions as is shown in Fig. 12a.

The infrasound intensities recorded during this event, however, cannot be described as low intensity. Therefore, there is an apparent contradiction between the decompression conditions of the magma recorded in the crystal textures and the actual intensity of the initial explosion. This can be explained by considering that the decompression histories recorded reflect the slow ascent and long residence of magma leftover from the May episode and that the exsolution of volatiles from the new intrusion of magma contributed to explosion intensity.

Our explanation implies that the majority of the magma ejected was the stalled magma that filled the conduit after the May activity and, more importantly, that the newly intruded magma itself contributed very little to the initial 14 July explosion. Instead, the fluxing of gas through the system from this new, deep intrusion likely added more gas over-pressure into an already over-pressurized system (Fig. 13). This means that two weeks after the signalled onset of the new intrusion, the gas over-pressure had reached critical levels, which eventually, at 06 h46 local time on 14 July, overcame the yield strength of the dense magma plug, blasting it apart and leading to the rapid decompression and evacuation of the top two kilometres of the conduit in a matter of minutes (Fig. 13). The magma that began its ascent during the last week of June continued rising in response to conduit evacuation, possibly contributing to the weeks of ash emissions and Strombolian activity after 14 July. Tilt data suggest that there was continued magma ascent throughout July–September, with only low-level surface activity including gas and ash venting and strombolian explosions. This activity culminated in another, although significantly less powerful (infrasound values of 3000 Pa; Hall et al., 2015), Vulcanian event on 18 October

2013, suggesting that the conduit did not seal itself before the 18 October event in a way that was as significant as before the 14 July event.

5.4. Explosion trigger and eruptive intensity

One main control of the effusive/explosive transition is magma ascent rate. Assuming that the June batch caused the October 18 explosion, the averaged ascent rate over this period is ~3 m h^{-1}. This is consistent with tilt signal modelling (Neuberg et al., 2018) but it is at the low end (Cassidy et al., 2018) of effusive eruptions with intermittent explosive activity, such as at Soufrière Hills (Edmonds et al., 2003), Unzen (Hirabayashi et al., 1995), Mt. St Helens (Gerlach and McGee, 1994), and Colima (Cassidy et al., 2015). This low ascent rate nevertheless gave rise to one of the most powerful recent event at Tungurahua. This apparent inconsistency, like that of microlite texture and infrasound intensity, constrains the possible mechanisms controlling eruption intensity. Our data show that large gas volumes were housed between the plug and the source region of the syn-explosive seismic activity at ~1.5 km depth (this study, Battaglia et al., 2019 and Kim et al., 2014). The explosive decompression of this zone was thus most likely responsible for propelling the fractured parts of the plug rock up to 4 km away from the vent during the initial explosion. Both these distances, which are in the high end of reported ballistic ranges for Vulcanian events (Isgett et al., 2017), and the high-intensity infrasound recorded during the explosions indicate very large pressure build-up and release. Our data show that the high tensile strength of the plug coupled with its extremely low porosity and permeability allowed such gas and pressure accumulation. We thus conclude that the presence of a well-developed high porosity zone was essential to initiate this powerful explosion.

The origin of other Vulcanian events have also been estimated as 1–2 km below the vent (Battaglia et al., 2019; Burgisser et al., 2011; Burgisser et al., 2010; Clarke et al., 2007) or shallower (Bain et al., 2018). Do such depths mark, as at Tungurahua, the lower bound of gas accumulation? Conduit porosity stratification has notably been determined at Soufrière Hills volcano (Burgisser et al., 2010). Since Tungurahua has no dome, the most appropriate comparison with Soufrière Hills is during late 1997, when a series of Vulcanian explosion occurred frequently enough to hinder dome formation prior to most explosions. Gas accumulation in the few hundred meters below the plug reached ~70 vol% porosity (Burgisser et al., 2011; Burgisser et al., 2010). This similarity with Tungurahua in gas content is encouraging, but the Soufrière Hills data were obtained by sampling multiple events to reconstruct conduit stratification. The shallow gas-rich regions of several explosions were thus combined in the reconstructed stratification. If these regions were at different levels, the apparent gas accumulation thickness of 400 to 700 m is a maximum estimate as it results from the superposition of gas-rich levels from separate events. Prior to the powerful Soufrière Hills event of 11 February 2010, the same conduit stratification reconstruction procedure from ejecta as we use herein suggests that gas accumulation below the plug did not exceed 10 vol% (Burgisser et al., 2019). While insufficient sampling cannot be ruled out as data suggested that no samples came from <300 m deep, a more likely explanation for the absence of high porosity storage at that time is that the trigger mechanism was unloading by dome collapse. On the other hand, at Merapi volcano, Indonesia, the 26 October 2010 explosive event featured a 20 vol% near-surface gas accumulation with a sharp porosity decrease between 0.5 and 1.5 km depth (Drignon et al., 2016; Komorowski et al., 2013). Likewise, the 5 November 2010 explosive event also featured a 20 vol% gas accumulation at 200–300 m depth with a sharp decrease at 1.1–1.7 km depth (Drignon et al., 2016; Komorowski et al., 2013). Both of these high-intensity events occurred at times of high ascent rates and featured a cryptodome and a surface dome, respectively. These values suggest that gas accumulated at <0.5 km depth and, the absence of a dome was correlated with higher degrees of gas accumulation. The simultaneous increase in the measured amount of SO$_2$ emitted, to >2500 t/day (Hidalgo et al., 2015), on the 14 July is fully consistent with large volumes of gas stored in the shallow conduit prior to explosion at Tungurahua. This opens the possibility that the presence of a dome makes large gas accumulation unnecessary for a powerful explosion. At Tungurahua, while the rise of the new magma batch promoted pressure build-up in the conduit, it is the decoupling of the gas from this new magma and the ensuing gas accumulation below the plug that conferred its intensity to the eruption.

6. Conclusions

Our analysis of a complete sample suite integrated with geophysical monitoring data from an unusually large Vulcanian explosion at Tungurahua, provided new insights into the intricate sequence of events that caused this explosion. Our study shows that the understanding of magma ascent dynamics and the processes that lead to the triggering of large Vulcanian events cannot be achieved without combining multiple disciplines. Our main results are:

- Geophysical data indicated a period of quiescence beginning towards the end of May 2013 with no magma ascent and continued low level degassing over a 6 week period.
- The intrusion of a new batch of magma into the edifice (at >3 km depth) was inferred from changes in the geophysical monitoring data (increase in tilt and seismicity) during the last week of June 2013.
- The explosion generated some of the largest ever recorded infrasound signal (> 5000 Pa) and a large amount of SO$_2$ (> 2500 t/day).
- The conduit was extensively vertically stratified with respect to porosity, permeability, crystallinity and volatile content prior to the 14 July 2013 Vulcanian explosion.
- A very dense (<2% porosity), but thin (< 50 m) plug of rock resided in the shallowest part of the conduit prior to the explosion. The matrix permeability of this plug is extremely low and its tensile strength high, creating a rigid effective seal against gas loss.
- There was a high porosity zone (> 50%) below the plug which acted as a gas storage region prior to the explosion.
- Feldspar microlite textures revealed that the decompression rates and undercooling in the magma during ascent were generally low and that the textures resulted from long residence times in the shallow conduit.
- The concurrence of slow ascent rates, the large infrasound intensity of the explosion, and the important shallow gas accumulation suggest that the newly intruded batch of magma was not directly involved in the Vulcanian event on 14 July 2013.
- We propose instead that volatile exsolution from the new batch of magma and gas fluxing through the conduit fed the shallow, high-porosity zone and led to significant gas over-pressure in the conduit.

The sequence of events leading to the 14 July explosion started immediately after the previous phase of activity in early May 2013. Due to a dwindling magma supply and increasing magma viscosity, remnants of the magma that ascended during that previous activity stalled in the conduit, triggering crystallization of the magma and the beginning of the formation of a dense plug, while closed system degassing continued in the magma column below. The intrusion of a new batch of magma deeper in the system triggered volatile exsolution and the fluxing of gas up into the shallow storage region. Pressurization was thus a result of gas accumulation and plug resistance to magma column extrusion in response to the new magma influx. On the 14th of July 2013, a critical gas-overpressure was reached. It overcame the strength of the dense plug, trigging rapid decompression and evacuation of the top few kilometres of the conduit. The new batch of intruded magma was not directly involved in the explosion. Geophysical data suggest that it continued to ascend, probably contributing to the low-level Strombolian activity and ash emissions in the following weeks, which

culminated in another, although much smaller, Vulcanian event on 18 October 2013.

CRediT authorship contribution statement

H. Elizabeth Gaunt: Conceptualization, Methodology, Formal analysis, Investigation, Writing - original draft, Writing - review & editing, Visualization.**Alain Burgisser:**Methodology, Formal analysis, Investigation, Writing - original draft, Writing - review & editing, Visualization.**Patricia A. Mothes:**Conceptualization, Resources, Writing - review & editing, Supervision.**John Browning:**Investigation, Resources, Writing - review & editing.**Philip G. Meredith:**Investigation, Resources, Writing - review & editing.**Evelyn Criollo:**Resources, Writing - review & editing.**Benjamin Bernard:**Resources, Writing - review & editing.

Declaration of competing interest

The authors declare that they have no known competing financial interests or personal relationships that could have appeared to influence the work reported in this paper.

Acknowledgements

References

Anderson, J.F., Johnson, J.B., Steele, A.L., Ruiz, M.C., Brand, B.D., 2018. Diverse eruptive activity revealed by acoustic and electromagnetic observations of the 14 July 2013 intense vulcanian eruption of Tungurahua Volcano, Ecuador. Geophys. Res. Lett. 45 (7), 2976–2985.

Andújar, J., Martel, C., Pichavant, M., Samaniego, P., Scaillet, B., Molina, I., 2017. Structure of the plumbing system at Tungurahua Volcano, Ecuador: insights from phase equilibrium experiments on July–August 2006 eruption products. J. Petrol. 58 (7), 1249–1278.

Bain, A.A., Calder, E.S., Cortés, J.A., Cortés, G.P., Loughlin, S.C., 2018. Textural and geochemical constraints on andesitic plug emplacement prior to the 2004–2010 vulcanian explosions at Galeras volcano, Colombia. Bull. Volcanol. 81 (1), 1.

Battaglia, J., Hidalgo, S., Bernard, B., Steele, A., Arellano, S., Acuña, K., 2019. Autopsy of an eruptive phase of Tungurahua volcano (Ecuador) through coupling of seismo-acoustic and SO2 recordings with ash characteristics. Earth Planet. Sci. Lett. 511, 223–232.

Bell, A.F., Naylor, M., Hernandez, S., Main, I.G., Gaunt, H.E., Mothes, P., Ruiz, M., 2018. Volcanic eruption forecasts from accelerating rates of drumbeat long-period earthquakes. Geophys. Res. Lett. 45 (3), 1339–1348.

Benson, P.M., Meredith, P.G., Platzman, E.S., 2003. Relating pore fabric geometry to acoustic and permeability anisotropy in Crab Orchard Sandstone: a laboratory study using magnetic ferrofluid. Geophys. Res. Lett. 30 (19).

Brugger, C.R., Hammer, J.E., 2010. Crystallization kinetics in continuous decompression experiments: implications for interpreting natural magma ascent processes. J. Petrol. 51 (9), 1941–1965.

Burgisser, A., Poussineau, S., Arbaret, L., Druitt, T.H., Giachetti, T., Bourdier, J.-L., 2010. Pre-explosive conduit conditions of the 1997 Vulcanian explosions at Soufrière Hills Volcano, Montserrat: I. Pressure and vesicularity distributions. J. Volcanol. Geotherm. Res. 194 (1–3), 27–41.

Burgisser, A., Arbaret, L., Druitt, T.H., Giachetti, T., 2011. Pre-explosive conduit conditions of the 1997 Vulcanian explosions at Soufrière Hills Volcano, Montserrat: II. Overpressure and depth distributions. J. Volcanol. Geotherm. Res. 199 (3–4), 193–205.

Burgisser, A., Bechon, T., Chevalier, L., Collombet, M., Arbaret, L., Forien, M., 2019. Conduit processes during the February 11, 2010 Vulcanian eruption of Soufrière Hills, Montserrat. J. Volcanol. Geotherm. Res. 373, 23–35.

Cassidy, M., Cole, P.D., Hicks, K.E., Varley, N.R., Peters, N., Lerner, A.H., 2015. Rapid and slow: varying magma ascent rates as a mechanism for Vulcanian explosions. Earth Planet. Sci. Lett. 420, 73–84.

Cassidy, M., Manga, M., Cashman, K., Bachmann, O., 2018. Controls on explosive-effusive volcanic eruption styles. Nat. Commun. 9 (1), 2839.

Clarke, A.B., Stephens, S., Teasdale, R., Sparks, R.S.J., Diller, K., 2007. Petrologic constraints on the decompression history of magma prior to Vulcanian explosions at the Soufrière Hills volcano, Montserrat. J. Volcanol. Geotherm. Res. 161 (4), 261–274.

Couch, S., Sparks, R.S.J., Carroll, M.R., 2003. The kinetics of degassing-induced crystallization at Soufriere Hills volcano, Montserrat. J. Petrol. 44 (8), 1477–1502.

Diller, K., Clarke, A.B., Voight, B., Neri, A., 2006. Mechanisms of conduit plug formation: Implications for vulcanian explosions. Geophys. Res. Lett. 33 (20), L20302.

Drignon, M.J., Bechon, T., Arbaret, L., Burgisser, A., Komorowski, J.C., Martel, C., Miller, H., Yaputra, R., 2016. Preexplosive conduit conditions during the 2010 eruption of Merapi volcano (Java, Indonesia). Geophys. Res. Lett. 43 (22), 11,595–511,602.

Edmonds, M., Oppenheimer, C., Pyle, D.M., Herd, R.A., Thompson, G., 2003. SO2 emissions from Soufriere Hills Volcano and their relationship to conduit permeability, hydrothermal interaction and degassing regime. J. Volcanol. Geotherm. Res. 124, 23–43.

Eichelberger, J.C., Carrigan, C.R., Westrich, H.R., Price, R.H., 1986. Nonexplosive silicic volcanism. Nature 323 (6089), 598–602.

Eychenne, J., Pennec, J.-L., Troncoso, L., Gouhier, M., Nedelec, J.-M., 2012. Causes and consequences of bimodal grain-size distribution of tephra fall deposited during the August 2006 Tungurahua eruption (Ecuador). Bull. Volcanol. 74 (1), 187–205.

Gaunt, H.E., Sammonds, P.R., Meredith, P.G., Smith, R., Pallister, J.S., 2014. Pathways for degassing during the lava dome eruption of Mount St. Helens 2004–2008. Geology 42 (11), 947–950.

Gerlach, T.M., McGee, K.A., 1994. Total sulfur dioxide emissions and pre-eruption vapor-saturated magma at Mount St. Helens, 1980–88. Geophys. Res. Lett. 21 (25), 2833–2836.

Ghiorso, M.S., Gualda, G.A.R., 2015. An H2O-CO2 mixed fluid saturation model compatible with rhyolite-MELTS. Contrib. Mineral. Petrol. 169, 53.

Giachetti, T., Druitt, T.H., Burgisser, A., Arbaret, L., Galven, C., 2010. Bubble nucleation, growth and coalescence during the 1997 Vulcanian explosions of Soufrière Hills Volcano, Montserrat. J. Volcanol. Geotherm. Res. 193 (3–4), 215–231.

Gualda, G.A.R., Ghiorso, M.S., Lemons, R.V., Carley, T.L., 2012. Rhyolite-MELTS: a modified calibration of MELTS optimized for silica-rich, fluid-bearing magmatic systems. J. Petrol. 53, 875–890.

Hall, M., Steele, A., Bernard, B., Mothes, P., Vallejo, S., Douillet, G., Ramón, P., Aguaiza, S., Ruiz, M., 2015. Sequential plug formation, disintegration by Vulcanian explosions, and the generation of granular Pyroclastic Density Currents at Tungurahua volcano (2013–2014), Ecuador. J. Volcanol. Geotherm. Res. 306, 90–103.

Hammer, J.E., Rutherford, M.J., 2002. An experimental study of the kinetics of decompression-induced crystallization in silicic melt. Journal of Geophysical Research: Solid Earth 107 (B1), 8–24 ECV 8-1-ECV.

Hammer, E.J., Cashman, V.K., Hoblitt, P.R., Newman, S., 1999. Degassing and microlite crystallization during pre-climactic events of the 1991 eruption of Mt. Pinatubo, Philippines. Bull. Volcanol. 60 (5), 355–380.

Hammer, J.E., Cashman, K.V., Voight, B., 2000. Magmatic processes revealed by textural and compositional trends in Merapi dome lavas. J. Volcanol. Geotherm. Res. 100 (1), 165–192.

Heap, M.J., Kennedy, B.M., 2016. Exploring the scale-dependent permeability of fractured andesite. Earth Planet. Sci. Lett. 447, 139–150.

Heap, M.J., Farquharson, J.I., Wadsworth, F.B., Kolzenburg, S., Russell, J.K., 2015. Timescales for permeability reduction and strength recovery in densifying magma. Earth Planet. Sci. Lett. 429, 223–233.

Hidalgo, S., Battaglia, J., Arellano, S., Steele, A., Bernard, B., Bourquin, J., Galle, B., Arrais, S., Vásconeza, F., 2015. SO2 degassing at Tungurahua volcano (Ecuador) between 2007 and 2013: transition from continuous to episodic activity. J. Volcanol. Geotherm. Res. 298, 1–14.

Hirabayashi, J.-i., Ohba, T., Nogami, K., Yoshida, M., 1995. Discharge rate of SO2 from Unzen Volcano, Kyushu, Japan. Geophys. Res. Lett. 22 (13), 1709–1712.

Isgett, S.J., Houghton, B.F., Fagents, S.A., Biass, S., Burgisser, A., Arbaret, L., 2017. Eruptive and shallow conduit dynamics during Vulcanian explosions: insights from the Episode IV block field of the 1912 eruption of Novarupta, Alaska. Bull. Volcanol. 79 (8), 58.

ISRM, 1978. Suggested methods for determining tensile strength of rock materials. International Journal of Rock Mechanics and Mining Sciences & Geomechanics Abstracts 15 (3), 99–103.

Jaupart, C., 1998. Gas Loss Through Conduit Walls During Eruption. Special Publications 145. Geological Society, London, pp. 73–90.

Kim, K., Lees, J.M., Ruiz, M.C., 2014. Source mechanism of Vulcanian eruption at Tungurahua Volcano, Ecuador, derived from seismic moment tensor inversions. Journal of Geophysical Research: Solid Earth 119 (2), 1145–1164.

Klug, C., Cashman, K.V., 1996. Permeability development in vesiculating magmas: Implications for fragmentation. Bull. Volcanol. 58 (2–3), 87–100.

Komorowski, J.-C., Jenkins, S., Baxter, P.J., Picquout, A., Lavigne, F., Charbonnier, S., Gertisser, R., Preece, K., Cholik, N., Budi-Santoso, A. and Surono, 2013. Paroxysmal dome explosion during the Merapi 2010 eruption: Processes and facies relationships of associated high-energy pyroclastic density currents. J. Volcanol. Geotherm. Res., 261: 260–294.

Martel, C., 2012. Eruption dynamics inferred from microlite crystallization experiments: application to Plinian and Dome-forming eruptions of Mt. Pelée (Martinique, Lesser Antilles). J. Petrol. 53 (4), 699–725. https://doi.org/10.1093/petrology/egr076.

Melnik, O., Sparks, R.S.J., 1999. Nonlinear dynamics of lava dome extrusion. Nature 402 (6757), 37–41.

Mollo, S., Hammer, J.E., 2017. Dynamic Crystallization in Magmas. European Mineralogical Union.

Morrissey, M., Mastin, L.G., 2000. Vulcanian Eruptions. In: Sigurdsson, H., Houghton, B., McNutt, S.R., Rymer, H., Stix, J. (Eds.), Encyclopedia of Volcanoes. Academic Press, pp. 463–475.

Neuberg, J.W., Collinson, A.S.D., Mothes, P.A., Ruiz, M.C., Aguaiza, S., 2018. Understanding cyclic seismicity and ground deformation patterns at volcanoes: intriguing lessons from Tungurahua volcano, Ecuador. Earth Planet. Sci. Lett. 482, 193–200.

Parra, R., Bernard, B., Narváez, D., Le Pennec, J.-L., Hasselle, N., Folch, A., 2016. Eruption Source Parameters for forecasting ash dispersion and deposition from vulcanian

eruptions at Tungurahua volcano: Insights from field data from the July 2013 eruption. J. Volcanol. Geotherm. Res. 309, 1–13.

Preece, K., Gertisser, R., Barclay, J., Charbonnier, S.J., Komorowski, J.-C., Herd, R.A., 2016. Transitions between explosive and effusive phases during the cataclysmic 2010 eruption of Merapi volcano, Java, Indonesia. Bull. Volcanol. 78 (8), 54.

Riker, J.M., Cashman, K.V., Rust, A.C., Blundy, J.D., 2015. Experimental Constraints on Plagioclase Crystallization during H 2 O- and H 2 O–CO 2 -Saturated Magma Decompression. J. Petrol. 56 (10), 1967–1998.

Romero, J.E., Douillet, G.A., Vallejo Vargas, S., Bustillos, J., Troncoso, L., Díaz Alvarado, J., Ramón, P., 2017. Dynamics and style transition of a moderate, Vulcanian-driven eruption at Tungurahua (Ecuador) in February 2014: pyroclastic deposits and hazard considerations. Solid Earth 8 (3), 697–719.

Shea, T., Hammer, J.E., 2013. Kinetics of cooling- and decompression-induced crystallization in hydrous mafic-intermediate magmas. J. Volcanol. Geotherm. Res. 260, 127–145.

Sparks, R.S.J., 1997. Causes and consequences of pressurisation in lava dome eruptions. Earth Planet. Sci. Lett. 150 (3–4), 177–189.

Stix, J., Torres, R., Narvaez, L., Cortes, G.P., Raigosa, J., Gomez, D., Castonguay, R., 1997. A model of vulcanian eruptions at Galeras volcano, Colombia. J. Volcanol. Geotherm. Res. 77 (1–4), 285–303.

Woods, A.W., Koyaguchi, T., 1994. Transitions between explosive and effusive eruptions of silicic magmas. Nature 370 (6491), 641–644.

Wright, H.M.N., Cashman, K.V., Rosi, M., Cioni, R., 2006. Breadcrust bombs as indicators of Vulcanian eruption dynamics at Guagua Pichincha volcano, Ecuador. Bull. Volcanol. 69 (3), 281–300.